Vortex beam generation by spin-orbit interaction with Bloch surface waves

(Article begins on next page)

24 April 2024

Vortex beam generation by spin-orbit interaction with Bloch surface waves

Ugo Stella, Thierry Grosjean, Natascia De Leo, Luca Boarino,
Peter Munzert, Joseph R. Lakowicz, and Emiliano Descrovi

Just Accepted

Vortex beam generation by spin-orbit interaction with Bloch surface waves

Ugo Stella[1], Thierry Grosjean[2], Natascia De Leo[3], Luca Boarino[3], Peter Munzert[4], Joseph R. Lakowicz[5] and Emiliano Descrovi[1]*

[1] Department of Applied Science and Technology (DISAT), Politecnico di Torino, Corso Duca degli Abruzzi 24, Torino, IT-10129, Italy.

[2] FEMTO-ST Institute, Université Bourgogne Franche-Comté, UMR CNRS 6174 15B Avenue des Montboucons, 25030, Besançon, France

[3] Quantum Research Labs & Nanofacility Piemonte, Advanced Materials Metrology and Life Science Division, Istituto Nazionale di Ricerca Metrologica (INRiM), Strada delle Cacce 91, Torino, IT-10135, Italy.

[4] Fraunhofer Institute for Applied Optics and Precision Engineering IOF, Albert-Einstein-Str. 7, Jena DE-07745, Germany

[5] Center for Fluorescence Spectroscopy, Department of Biochemistry and Molecular Biology, University of Maryland School of Medicine, Baltimore, Maryland 21201, United States

Mr. Ugo Stella: ugo.stella@polito.it

Dr. Thierry Grosjean: thierry.grosjean@univ-fcomte.fr

Dr. Natascia De Leo: n.deleo@inrim.it

Dr. Luca Boarino: l.boarino@inrim.it

Dr. Peter Munzert: peter.munzert@iof.fraunhofer.de

Prof. Joseph R. Lakowicz: JLakowicz@som.umaryland.edu

Corresponding Author:

Prof. Emiliano Descrovi: emiliano.descrovi@polito.it

Phone: +39 011 090 7352

Fax: +39 011 090 7399

Keywords: Chiral nanostructures, Bloch Surface Waves, vortex beam, spiral diffraction gratings, azimuthally polarized beam.

33 **ABSTRACT**

34 Axis-symmetric grooves milled in metallic slabs have been demonstrated to promote the transfer of

35 Orbital Angular Momentum (OAM) from far- to near-field and vice versa, thanks to spin-orbit

36 coupling effects involving Surface Plasmons (SP). However, the high absorption losses and the

37 polarization constraints, which are intrinsic in plasmonic structures, limit their effectiveness for

38 applications in the visible spectrum, particularly if emitters located in close proximity to the metallic

39 surface are concerned. Here, an alternative mechanism for vortex beam generation is presented,

40 wherein a free-space radiation possessing OAM is obtained by diffraction of Bloch Surface Waves

41 (BSWs) on a dielectric multilayer. A circularly-polarized laser beam is tightly focused on the

42 multilayer surface by means of an immersion optics, such that TE-polarized BSWs are launched

43 radially from the focused spot. While propagating on the multilayer surface, BSWs exhibit a spiral-

44 like wavefront due to the Spin-Orbit Interaction (SOI). A spiral grating surrounding the illumination

45 area provides for the BSW diffraction out-of-plane and imparts an additional azimuthal geometric

46 phase distribution defined by the topological charge of the spiral structure. At infinity, the

47 constructive interference results into free-space beams with defined combinations of polarization and

48 OAM satisfying the conservation of the Total Angular Momentum, based on the incident polarization

49 handedness and the spiral grating topological charge. As an extension of this concept, chiral

50 diffractive structures for BSWs can be used in combination with surface cavities hosting light sources

51 therein.

1
2
3
4   52   Vortex beams represent a family of structured beams generally characterized by a phase singularity
5
6   53   along the optical axis, a doughnut intensity distribution and an azimuthally-varying phase over a beam
7
8   54   transverse cross-section.[1,2] When the polarization state is spatially inhomogeneous, the term Vectorial
9
10 55   Vortex Beams is often used.[3] From a quantum-optics perspective, each vortex beam photon is
11
12
13 56   provided with a quantized Orbital Angular Momentum (OAM) equal to $\hbar\ell$, where ℓ is either a
14
15 57   positive or negative integer indicating the topological charge of the vortex. In recent years, vortex
16
17 58   beams have gained an increasing popularity because of several new applications into different
18
19
20 59   domains such as micro-particle manipulation and trapping,[4-6] compact laser sources,[7,8] microscopy[9,10]
21
22 60   and optical communications.[11,12] Conventional methods for producing vortex beams[13] involve the
23
24 61   use of (possibly tunable) anisotropic media such as Liquid Crystal[14,15] and q-plates[16] or hierarchically
25
26 62   structured holograms encoding proper phase functions.[17-20] More recently, metasurfaces, which can
27
28
29 63   be either dielectric or plasmonic, have been introduced in order to gather more degrees of freedom in
30
31 64   OAM manipulation,[21,22] through the control of the so-called Spin-Orbit Interaction (SOI)[23] mediated
32
33 65   by the metasurface topology .[24] Metasurfaces are mainly employed as free-space beam converters,
34
35
36 66   which have found applications also within laser cavities.[25] The concept of beam conversion through
37
38 67   metasurfaces relies on a spatially-dependent phase manipulation of the scattered field. The output
39
40 68   vortex beams result from a coherent sum of the scattered radiation originating from different portions
41
42
43 69   of the surface, which is illuminated as a whole. Despite the very high-efficiency capabilities for
44
45 70   generating vortex beams both in transmission[26,27] and reflection, [28] metasurface-based approaches can
46
47 71   be hardly adopted when the input field has a limited spatial extension (as for localized sources), unless
48
49 72   some collective mode coupling is intervening. [29] This is indeed the case in structured metallic films,
50
51
52 73   wherein the generation of free-space vortex beam carrying OAM occurs upon SOI and
53
54 74   scattering/diffraction of plasmonic modes by means of nano-slits,[30,31] properly arranged nano-
55
56 75   apertures,[32] possibly combined with circular[33,34] or spiral[35]diffraction gratings. Such results rely on
57
58 76   the fact that the Angular Momentum (AM) possessed by surface plasmons can be further manipulated
59
60
    77   and transferred to freely propagating radiation.[31,35]

78 Here we propose an alternative way of producing vortex beam, by exploiting Bloch Surface Waves

79 (BSW)[36,37] on dielectric multilayers as a mean to transfer energy, momentum and AM to a free-space

80 propagating beam. Such a two-step process involves a Spin Angular Momentum (SAM)-to-OAM

81 conversion from a focused circularly polarized beam into radially propagating BSWs and a BSW

82 diffraction in free-space, with the additional phase distribution imparted by a chiral diffraction grating.

83 Such a BSW-based approach can benefit from the multilayer low absorption that is potentially

84 suitable for light source integration and an additional degree of freedom in the polarization state of

85 coupled BSWs, which can be either TE- or TM-polarized depending on the multilayer design.[38] For

86 example, a directional coupling of BSWs promoted by a magnetic spin-orbit interaction has been

87 recently demonstrated.[39]

88 The setup and the sample structure are shown in Figure 1 and described in detail in the Methods

89 section. Briefly, in Figure 1a, a circularly polarized Gaussian CW laser beam (λ=532 nm) is expanded

90 and spatially filtered by means of a properly sized circular Beam Blocker. An oil-immersion, high

91 NA objective is back-contacted to a multilayer glass substrate, in order to focus the incoming beam

92 onto a flat area of the top surface, surrounded by a periodic annular grating. The multilayer is made

93 of a stack of multiple Ta_2O_5 and SiO_2 layers, topped by a 75 nm-thick PMMA film (Figures 1b,c).

94 Thanks to the beam blocker, only focused light propagating at angles larger than the glass/air critical

95 angle θ_c can reach the sample. A fraction of the incoming power is thus available for coupling to

96 BSWs, provided that wavelength, momentum and polarization matching conditions are fulfilled, as

97 indicated by the BSW dispersion curve for TE-polarization.[40] The transverse size of the focused spot

98 is sub-micron, while the central flat area surrounded by the annular grating is 6 μm wide, such that

99 the grating plays no role in the BSW coupling. Since the coupling mechanism is polarization-

100 dependent and the incident electric field is circularly polarized, BSWs are spreading radially from the

101 focused spot area, with an accumulated phase delay that is linearly varying with the azimuthal angle

102 of the propagation direction. As a result of the SAM-to-OAM transfer, a BSW propagating radially

103   on the multilayer surface is obtained, with a peculiar spiral-like wavefront profile (see Supporting

104   Information), analogous to plasmonic vortices.[41] Surrounding the flat coupling region, a diffractive

105   grating is etched in the PMMA layer. The grating operates as an outcoupler, by diffracting BSWs

106   out-of-plane in both substrate (glass) and cladding (air) media, along a direction close-to-normal to

107   the sample surface (order of diffraction n=-1).[42] Depending on the grating shape (e.g. circular or

108   spiral-like), an additional phase profile can be imparted to the diffracted radiation. In previous

109   applications, this feature has been exploited for steering the diffracted beam.[43,44] The outcoupled

110   power is then collected by the same high-NA objective and Fourier-transformed before being imaged

111   on the camera plane. A linear polarizer and a quarter-wave plate allow for a polarization analysis on

112   the collected images. If the beam blocker is removed, an interference pattern as shown in Figure 1a

113   can be obtained. In this example, the spiral-shaped interference fringes result from the superposition

114   of a diffracted vortex beam (charge $\ell = 1$) and light reflected from the sample surface.[35]

[FIGURE 1]

Figure 1. a) Sketch of the experimental setup. L1-4 Plano-Convex lenses, $LP_{1,2}$ Polarizers, $QW_{1,2}$ Quarter-wave Plates, BB Beam Blocker, BS Beamsplitter, BFP Back Focal Plane. In the exemplary BFP image, an interference pattern is shown, due to the superposition of a diffracted vortex beam and a reflected spherical wave from the sample surface. No Beam Blocker has been used in this case. b) Detailed view of the BSW coupling and diffraction mechanism. Illumination is provided by means of a beam-blocked circularly polarized laser beam focused through an oil immersion objective, such that the minimum incidence angle is slightly above the critical angle θ_c, in order to match the BSW coupling conditions. c) Sketch of the multilayer structure with an exemplary spiral diffraction grating fabricated in PMMA on top (not to scale).

RESULTS AND DISCUSSION

127   In this section, experimental results are presented related to (i) a circular-symmetric annular grating

128   with topological charge m=0, (ii) a single-arm spiral grating, (iii) a double-arm spiral grating. In the

129   last two cases, both handedness of the incident polarization are considered, namely Right-Handed

130   Circular (RHC) and Left-Handed Circular (LHC) polarizations, such that the incident beam SAM and

5

1
2
3
4   131   the grating topological charge can have either equal or opposite sign. In order to evaluate the
5
6   132   polarization state of the diffracted light, the polarization ellipse parameter $\varepsilon(k_x,k_y) = \frac{1}{2}arg$
7
8
9   133 $\left(\sqrt{S_1^2 + S_2^2} + iS_3\right)$ is calculated across the Back Focal Plane (BFP), where S_1, S_2 and S_3 are the Stokes
10
11   134   parameters.[45] Right-Handed Circular (RHC), Left-Handed Circular (LHC) and Linear Polarizations
12
13
14   135   (LP) correspond to $\varepsilon_{RHC} = \frac{\pi}{4}$, $\varepsilon_{LHC} = -\frac{\pi}{4}$ and $\varepsilon_{LP} = 0$ respectively. Polarization-filtered raw images
15
16
17   136   and Stokes parameter distributions for the structures considered here are shown in the Supporting
18
19   137   Information.
20
21   138   A numerical 3D model based on a commercial Finite-Difference Time-Domain (FDTD) solver
22
23   139   (Lumerical Inc.) is used to support the interpretation of the experimental observations. In order to
24
25   140   mimic the focused circularly polarized beam underlying the BSW coupling, a pair of (coherent) linear
26
27
28   141   orthogonal dipoles laying on the multilayer plane and oscillating with a $\frac{\pi}{2}$ relative phase delay are
29
30
31   142   introduced (see Supporting Information Movie S2). Further details on the validity of this model are
32
33   143   provided in the Methods section.
34
35
36   144   **Circular Outcoupler (m=0).** In this configuration, a RHC circular polarization ($\varepsilon = \frac{\pi}{4}$) is employed
37
38   145   to couple BSWs that are then diffracted. As shown in Figures 2a,e, the total intensity collected on
39
40
41   146   the BFP exhibits a maximum at $k_x=k_y=0$, corresponding to a constructive interference condition for
42
43   147   light traveling along a direction perpendicular to the multilayer surface. A linear-polarization filtering
44
45   148   reveals the presence of a pair of spiral-like fringes spreading from the central maximum that rotate as
46
47
48   149   the polarization analyser is rotated (in Figures 2b,f the measured and calculated intensity of the x-
49
50   150   component of the diffracted light are presented). Without the polarization filter, the spiral-like fringes
51
52   151   merge together to form a ring surrounding the central maximum. When polarization-projected onto a
53
54   152   RHC polarization state, the intensity pattern has still a maximum in the BFP center (Figures 2c,g),
55
56
57   153   while a weak ring is obtained for a projection onto a LHC polarization state (Figures 2d,h). A
58
59   154   comparison between the distributions for the measured and the calculated parameter $\varepsilon(k_x,k_y)$ on the
60

6

155   BFP indicates that the central maximum is substantially RHC polarized, i.e. $\varepsilon(0,0) \cong \frac{\pi}{4}$. The

156   polarization state is smoothly flipping to LHC (i.e. $\varepsilon(0,0) \cong -\frac{\pi}{4}$) while moving radially from the

157   center (Figures 2i,l).

158   By enforcing the conservation of the Total Angular Momentum J, which also takes into account the

159   topological charge m imparted by the diffraction grating, the following equation applies: $\sigma_i + m =$

160   $1 + 0 = \sigma_o + \ell$, where σ_o is the output SAM number and ℓ is the corresponding OAM number. The

161   solution to this equation is not unique. In particular, two SAM-OAM configurations are possible: a

162   RHC beam preserving the input polarization and carrying zero OAM, i.e. $\sigma_o = +1$ and $\ell = 0$, and a

163   doughnut LHC beam with a reverse polarization, with $\sigma_o = -1$ and OAM with $\ell = +2$. The two

164   beams are partially overlapped, thus explaining the polarization state change from RHC to LHC along

165   a radial direction,[35] as illustrated above. This observation is supported by the phase distribution

166   calculated for the RHC and the LHC polarized fields presented in Figures 2m,n: a flat wavefront with

167   constant phase is found for the RHC beam ($\ell = 0$) and a spiral wavefront with two 2π discontinuities

168   for the LHC beam ($\ell = +2$).

169   [FIGURE 2]

170   **Figure 2**. BFP Diffraction patterns from a circular outcoupler ($m = 0$). Incident polarization is RHC.

171   a,e) experimental and calculated total intensity showing a central spot surrounded by a weak outer

172   ring; b,f) experimental and calculated x-polarized intensity; c,g) experimental and calculated RHC

173   intensity showing a central spot; d,h) experimental and calculated LHC intensity showing a doughnut

174   shape; i,l) experimental and calculated polarization ellipse parameter $\varepsilon(k_x, k_y)$ with the sign reversal

175   from the inner area to the outer ring; m) calculated phase of the diffracted field with RHC polarization,

176   showing a constant distribution; n) calculated phase of the diffracted field with LHC polarization,

177   showing two 2π discontinuities (vortex charge $\ell = +2$).

178

179   **Spiral Outcoupler ($m = -1$)**. BSWs are first coupled with an input RHC polarization ($\sigma_i = +1$)

180   and made interacting by a spiral grating with opposite handedness ($m = -1$). The corresponding

181   intensity pattern is shown in Figures 3a,e.

7

[FIGURE 3]

Figure 3. BFP Diffraction patterns from a 1-arm spiral outcoupler ($m = -1$). Incident polarization is RHC. a,e) experimental and calculated total intensity showing a doughnut shape; b,f) experimental and calculated x-polarized intensity; c,g) experimental and calculated y-polarized intensity; d,h) experimental and calculated 45°-polarized intensity; i,l) experimental and calculated polarization ellipse parameter $\varepsilon(k_x,k_y)$ indicating a substantially linear polarization state $\varepsilon\cong0$; m,n) experimental and calculated ellipse parameter $\alpha(k_x,k_y)$ indicating an azimuthal orientation of the electric field.

The phase delay profile imparted by the diffractive structure onto the diffracted BSWs results in a destructive interference such that a zero-intensity phase singularity is produced at $k_x=k_y=0$. When filtered with the linear polarizer LP_1 (e.g. oriented along the x, y or 45° direction), two-lobe patterns are found, whose orientation is perpendicular to the analyzer transmission axis (Figures 3b-d). Calculated intensity patterns are in good agreement with the experimental observations (Figures 3f-h). The distribution of the parameter $\varepsilon(k_x,k_y)$ shows a substantially linear polarization corresponding to the doughnut ($\varepsilon\cong0$) (Figures 3i,l). The uniformity of the polarization orientation is evaluated by extracting the parameter $\alpha(k_x,k_y) = \frac{1}{2}arg(S_1 + iS_2)$, which provides the local orientation of the polarization ellipse (almost a line, in this case) across the BFP.[45] In Figures 3m,n both the experimental and the calculated distributions for $\alpha(k_x,k_y)$ indicate that the substantially linear polarization follows an axis-symmetric distribution such that the electric field is azimuthally oriented about the beam axis in $k_x = k_y = 0$. In this case, the J conservation rule reads as $\sigma_i + m = 1 - 1 = \sigma_o +\ell = 0$, leading to two fully overlapped beams with SAM $\sigma_o = +1$ and OAM $\ell = -1$ and $\sigma_o = -1$ and OAM $\ell = +1$, respectively (see Figures S6e,f and Figures S7e,f in Supporting Information). The coherent superposition of such beams having circular, yet orthogonal, polarizations is consistent with the observed azimuthal polarization state of the output beam.

When the illumination polarization is switched to LHC ($\sigma_i = -1$) the input SAM and the grating topological charge possess the same sign. The overall intensity pattern having a doughnut shape is

208   presented in Figures 4a,e. At a closer look, the output results from the superposition of a pair of ring-

209   shaped beams, which are non-interfering because of their orthogonal polarizations. A weak outer ring

210   (Figures 4c,g) is imaged upon RHC filtering, while an intense inner ring (Figures 4d,h) is obtained

211   upon LHC filtering. The experimental and the calculated distributions for $\varepsilon(k_x,k_y)$ (Figures 4i,l)

212   confirm that the polarization state of the two beams is still substantially circular. However, a reversal

213   of handedness from LHC to RHC can be found while moving from the inner ring toward the outer.

214   The two partially overlapped beams must satisfy the J conservation rule, i.e. $\sigma_i + m = -1 - 1 = \sigma_o$

215   $+\ell = -2$. A first solution to this equation is represented by a LHC polarized beam having the same

216   SAM number as the incident radiation $\sigma_o = -1$ and OAM $\ell = -1$ (Figures 4d,h). An orthogonal

217   solution is a RHC polarized beam having a reversed SAM $\sigma_o = +1$ and OAM $\ell = -3$ (Figures 4c,g).

218   The topological charge of the diffracted vortex beams can be directly appreciated from the calculated

219   phase distributions of the RHC and LHC polarized beams (Figures 4m,n), exhibiting three and one

220   2π discontinuities respectively, on the BFP.

221   [FIGURE 4]

222   **Figure 4**. BFP Diffraction patterns from a 1-arm spiral outcoupler ($m = -1$). Incident polarization is

223   LHC. a,e) experimental and calculated total intensity showing a superposition of an inner and an outer

224   ring-shaped patterns; b,f) experimental and calculated x-polarized intensity; c,g) experimental and

225   calculated RHC intensity, distributed according to the outer ring; d,h) experimental and calculated

226   LHC intensity; distributed according to the inner ring; i,l) experimental and calculated polarization

227   ellipse parameter $\varepsilon(k_x,k_y)$ indicating a substantially circular polarization with handedness reversal

228   from the inner to the outer ring; m) calculated phase of the diffracted field with RHC polarization,

229   showing three 2π discontinuities; n) calculated phase of the diffracted field with LHC polarization,

230   showing one 2π discontinuity.

231

232   **Spiral Outcoupler ($m = -2$)**. As in the previous configuration, an incident RHC polarization (σ_i

233   $= +1$) is first considered. The overall intensity shown in Figures 5a,e is obtained as the superposition

234   of a weak outer ring and a brighter central spot. Both patterns can be individually imaged by operating

235 a polarization filtering through a RHC state (Figures 5c,g) and a LHC state (Figures 5d,h),

236 respectively.

237   [FIGURE 5]

238 **Figure 5**. BFP Diffraction patterns from a 2-arms spiral outcoupler ($m = -2$). Incident polarization

239 is RHC. a,e) experimental and calculated total intensity, given by the superposition of a central spot

240 an a weaker outer ring; b,f) experimental and calculated x-polarized intensity; c,g) experimental and

241 calculated RHC intensity, distributed according to the weak outer ring; d,h) experimental and

242 calculated LHC intensity, distributed according to the bright central spot; i,l) experimental and

243 calculated polarization ellipse parameter $\varepsilon(k_x,k_y)$ indicating a substantially circular polarization, with

244 handedness reversal from the central spot to the outer ring; m) calculated phase of the diffracted field

245 with RHC polarization, showing two 2π discontinuities (vortex charge $\ell = -2$); n) calculated phase

246 of the diffracted field with LHC polarization, showing a uniform phase distribution (vortex charge

247 $\ell = 0$).

248

249 The distribution of the parameter $\varepsilon(k_x,k_y)$ indicates that the polarization is substantially circular

250 across the pattern. However, the bright central spot shows a LHC polarization state, which is reversed

251 with respect to the incident radiation (Figure 5i). Furthermore, the outer weak ring maintains a LHC

252 polarization, as the illumination (Figure 5l). The conservation of the momentum J leads to $\sigma_i + m =$

253 $+1 - 2 = \sigma_o + \ell = -1$, which has the following two solutions associated to the observed beams: σ_o

254 $= +1$ (RHC) and $\ell = -2$; $\sigma_o = -1$ (LHC) and $\ell = 0$. The calculated phase distributions are

255 consistent with the Total Angular Momentum algebra, since the RHC beam has a vortex wavefront

256 with two 2π discontinuities, while the LHC beam has a flat wavefront (Figures 5m,n). A constant

257 phase is also consistent with the existence of a central maximum at $k_x = k_y = 0$ for the LHC beam

258 (similar situation as in Figure 2m, with a RHC polarization).

259 For a LHC polarization ($\sigma_i = -1$) a phase singularity is produced on the optical axis, and the overall

260 intensity pattern (Figures 6a,e) results from the superposition of a RHC polarized vortex of charge

261 $\ell = -4$ (Figures 6c,g,m) and a LHC polarized vortex of charge $\ell = -2$ (Figures 6d,h,n).

262

263   [FIGURE 6]

264   **Figure 6**. BFP Diffraction patterns from a 2-arm spiral outcoupler ($m = -2$). Incident polarization is

265   LHC. a,e) experimental and calculated total intensity; b,f) experimental and calculated x-polarized

266   intensity; c,g) experimental and calculated RHC intensity; d,h) experimental and calculated LHC

267   intensity; i,l) experimental and calculated polarization ellipse parameter $\varepsilon(k_x, k_y)$; m) calculated phase

268   of the diffracted field with RHC polarization showing four 2π discontinuities (vortex charge $\ell = -$

269   4); n) calculated phase of the diffracted field with LHC polarization, showing two 2π discontinuities

270   (vortex charge $\ell = -2$).

271

272   Measured and calculated $\varepsilon(k_x, k_y)$ show the handedness reversal occurring when departing from the

273   optical axis toward larger propagation angles, wherein the inner ring preserves the same polarization

274   handedness as the incident radiation (Figures 6i,l). From the conservation of the momentum J, we

275   have: $\sigma_i + m = -1 - 2 = \sigma_o + \ell = -3$, whose solutions are: $\sigma_o = +1$ (RHC) and $\ell = -4$; $\sigma_o = -1$

276   (LHC) and $\ell = -2$, in accordance to the results shown in Figure 6.

277

278   **CONCLUSION**

279   To conclude, a new mechanism for the generation of vectorial vortex beams has been presented, based

280   on spin-orbit interactions involving coupling and diffraction of BSWs. Generally speaking, this kind

281   of effects relies on the coherence characteristics of the radiation involved. For this reason, we

282   employed a laser beam as an external free-space radiation for coupling BSWs that are subsequently

283   diffracted, with an imparted azimuthal phase profile. Several combinations of polarization states and

284   OAM are obtained, as summarized in Table 1. Further options for vortex beam generation carrying

285   OAM with other polarization configurations can be possibly produced by means of multilayers

286   supporting TM-polarized, in addition to TE-polarized BSWs.[46] Moreover, the efficiency of the vortex

287   beam generation can be improved by properly shaping the angular spectrum of the incident radiation,

288   for example as a Bessel beam.[47]

	Grating Topological Charge m	$m = 0$	$m = -1$	$m = -2$
Incident SAM σ_i				
$\sigma_i = +1$		$\sigma_o = -1 \ \& \ \ell = +2$ $\sigma_o = +1 \ \& \ \ell = 0$	$\sigma_o = -1 \ \& \ \ell = +1$ $\sigma_o = +1 \ \& \ \ell = -1$	$\sigma_o = -1 \ \& \ \ell = 0$ $\sigma_o = +1 \ \& \ \ell = -2$
$\sigma_i = -1$		$\sigma_o = -1 \ \& \ \ell = 0$ $\sigma_o = +1 \ \& \ \ell = -2$	$\sigma_o = -1 \ \& \ \ell = -1$ $\sigma_o = +1 \ \& \ \ell = -3$	$\sigma_o = -1 \ \& \ \ell = -2$ $\sigma_o = +1 \ \& \ \ell = -4$

Table 1. Summary of the SAM-OAM combinations obtained by diffraction of BSWs coupled from either RHC or LHC polarized incident light.

The numerical model developed here suggests that the presented approach is likely to work regardless of the coupling mechanism for BSWs. For example, in the perspective of advanced engineered light sources for free-space applications, BSWs can be launched from a single emitter on the multilayer surface by virtue of near-field interactions (so-called BSW-coupled emission).[48,49] Then, chiral diffractive structures can be used as outcouplers surrounding single point-like sources or even planar BSW cavities (e.g. as described in ref.[50]) hosting light sources within. Provided the coherence requirements for the BSW-coupled radiation leaking out of the cavity are satisfied, the diffraction mechanism for free-space vortex generation remains as reported in the text above. While cavities can be chiral themselves, with a handedness-depending Local Density of States,[51] it has been recently shown that chiral plasmonic structures can foster sources located on their surface to radiate according to a specific circular polarization handedness.[52] These strategies provide an unprecedented degree of control on the polarization state of the emitted light. The use of BSWs as a mean for coupling and transferring energy from sources to free-space, mediated by chiral diffractive gratings, can contribute to enhance the performance of purely plasmonic nanostructures, which are often limited by the strong absorption of metals occurring at visible frequencies.

12

1
2
3
4
5
6
7
8
9
10
11
12
13
14
15
16
17
18
19
20
21
22
23
24
25
26
27
28
29
30
31
32
33
34
35
36
37
38
39
40
41
42
43
44
45
46
47
48
49
50
51
52
53
54
55
56
57
58
59
60

METHODS

310

311 **Experimental setup.** A TEM_{00} doubled-frequency Nd:YAG laser beam (GEM, Laser Quantum) is

312 collimated (L_1) and transmitted through a first polarization-control box, consisting of a linear

313 polarizer LP_1 and a quarter wave plate QW_1. Circular polarization states with both handedness (RH

314 and LH) are generally produced. A beam blocker is introduced in order to spatially filter the laser

315 beam, such that an illumination above the glass/air critical angle θ_c is provided only. The incoming

316 beam is focused onto a flat area on the top surface of the multilayer through a $NA = 1.49$ objective

317 (Nikon Apo TIRF 1003) that is back-contacted to the glass substrate of the sample. The focused spot

318 has a transverse size much smaller than the diameter of the central flat region of the grating. In this

319 way, the BSW coupling mechanism is resulting from a momentum-matching condition solely ruled

320 by refraction. The sample holder is mounted on a 3-axis piezo stage. When measuring the diffraction

321 patterns from the spiral gratings, the excitation laser is accurately focused onto the geometric center

322 of the diffraction gratings. Diffracted light on the glass side is collected by the same objective and

323 directed toward the collection arm of the setup, after passing through a 50/50 beam splitter. A second

324 polarization-control box consisting of a quarter wave plate QW_2 and a linear polarizer LP_2 filters the

325 outgoing wave onto the desired polarization state (RHC, LHC or LP). Subsequently, the lens L4

326 images the BFP of the objective onto a CMOS camera (Thorlabs HR-CMOS DCC3260M). With no

327 Beam Blocker, an interference pattern appears in the BFP image, due to the superposition of the light

328 reflected by the multilayer inside the light cone ($NA \leq 1$) with the diffracted BSW patterns,

329 eventually carrying OAM. As a result, spiral-like interference fringes can be observed depending on

330 the OAM number ℓ, as shown in Figure S3.[35]

331 **Sample fabrication.** The 1DPC consists of a dielectric multilayer made of a stack of Ta_2O_5 (high

332 refractive index) and SiO_2 (low refractive index) layers, deposited on a glass coverslip (150 μm

333 thickness) by plasma ion-assisted deposition under high vacuum conditions (APS904 coating system,

334 Leybold Optics). The stack sequence is substrate-[Ta_2O_5-SiO_2]x6-Ta_2O_5-SiO_2-PMMA with 15 layers

335 in total, including PMMA. The Ta_2O_5 layer (refractive index n_{Ta2O5}=2.08) is 95 nm thick, the SiO_2

13

336 layer (refractive index n_{SiO2}=1.46) is 137 nm thick. The top SiO_2 layer on top of the stack is 127 nm

337 thick. On top of the structure a 75 nm thick layer of PMMA is spun for pattern fabrication

338 (n_{PMMA}=1.48). Chiral diffractive structures are fabricated by electron beam lithography.

339 **Numerical modeling.** Numerical modeling is performed using the Finite-Difference Time-Domain

340 method in the Lumerical Inc. software. In order to mimic the focused circularly polarized light

341 coupling to BSWs, a pair of orthogonal dipolar emitters are positioned at the geometric center of the

342 spiral grating. More specifically, the emitters are placed 10 nm above the PMMA layer, with the

343 dipole momentum laying parallel to the multilayer surface, such that the TE polarization of the BSW

344 can be matched. The two oscillators are phase-shifted by $\pm \pi/2$. In this way, thanks to a near-field

345 interaction, part of the radiated energy from the dipoles is transferred to BSWs (BSW-coupled

346 emission). As shown in Figure S1 and Supporting Movie S2, resulting BSWs are radially propagating,

347 with a spiral wavefront due to the time-varying polarization matching conditions of the field given

348 by the coherent sum of the radiation from the two dipoles.

349 The diffraction gratings are modeled as circular or spiral grooves in the PMMA layers, with a spatial

350 period Λ=450 nm. The total simulation region has dimensions $(15 \times 15 \times 2.6)$ μm^3. Boundary

351 conditions are set as perfectly matched layers. The smallest mesh size is 23 nm. The electromagnetic

352 near-field is collected using a spatial monitor over a plane 20 nm above the PMMA layer. A near-to

353 far-field projection technique is applied to calculate the field at a distance of 1 m from the structure,

354 on the air side. A cylindrical Perfect Electric Conductor, placed 50 nm above the dipole sources, have

355 been introduced in order to avoid the direct free-space emission from the sources, which could

356 produce interference with the BSW-diffracted radiation we want to investigate. This metallic plate

357 mimic the role of the Beam Blocker in the experimental setup. With this arrangement, only the air-

358 side far-field patterns are calculated. However, as the propagation angles of the diffracted beams (with

359 respect to the multilayer normal) are very small, the refraction effects are negligible and the far-field

360 patterns are expected to be similar to those on the glass substrate side.

361

14

1
2
3 362 **ACKNOWLEDGEMENTS**
4
5 363
14
   368
15
16 369 **SUPPORTING INFORMATION**
17
18 370 - 3D model of the geometry employed in FDTD simulations, interference patterns for vortex beams
19
20 371 with different topological charges, experimental and calculated polarization-filtered intensities and
21
22 372 corresponding Stokes parameter distributions of diffracted vortex beams (PDF).
23
24 373 - Calculated FDTD propagation of the BSW electric field coupled from a pair of $\pi/2$-phase delayed
25
   374 orthogonal dipoles on a flat multilayer surface (MP4).
26
27
28
29
30
31
32
33
34
35
36
37
38
39
40
41
42
43
44
45
46
47
48
49
50
51
52
53
54
55
56
57
58
59
60

15

REFERENCES

(1)   Yao, A.M.; Padgett. M.J. Orbital angular momentum: origins, behavior and applications. *Adv. Opt. Photon.* **2011**, 3, 161-204.

(2)   Shen, Y.; Wang, X.; Xie, Z.; Min,C.; Fu, X.; Liu Q.; Gong, M.; Yuan, X. Optical vortices 30 years on: OAM manipulation from topological charge to multiple singularities. *Light: Science & Applications* **2019**, 8, 90.

(3)   Yi, X.; Liu, Y.; Ling, X.; Zhou, X.; Ke, Y.; Luo, H.; Wen, S.; Fan, D. Hybrid-order Poincare sphere. *Physical Review A* **2015**, 91, 023801.

(4)   Ng, J.; Lin, Z.; Chan, C.T. Theory of Optical Trapping by an Optical Vortex Beam. *Physical Review Letters* **2010**, 104, 103601.

(5)   Cojoc, D.; Garbin, V.; Ferrari, E.; Businaro, L.; Romanato, F.; Di Fabrizio, E. Laser trapping and micro-manipulation using optical vortices, *Microelectronic Engineering* **2005**, 78–79,125-131.

(6)   Ma, Y.; Rui, G.; Gu, B.; Cui, Y. Trapping and manipulation of nanoparticles using multifocal optical vortex metalens. *Scientific Reports* **2017**, 7, 14611.

(7)   Cai, X.; Wang, J.; Strain, M.J.; Johnson-Morris, B.; Zhu, J.; Sorel, M.; O'Brien, J.L.; Thompson, M.G.; Yu, S. Integrated compact optical vortex beam emitters. *Science* **2012**, 6, 338-363.

(8)   Xie, Z.; Lei, T.; Li, F.; Qiu, H.; Zhang, Z.; Wang, H.; Min, C.; Du, L.; Li, Z.; Yuan, X. Ultra-broadband on-chip twisted light emitter for optical communications. *Light: Science & Applications* **2018**, 7, 18001

(9)   Wei, S.; Lei, T.; Du, L.; Zhang, C.; Chen, H.; Yang, Y.; Zhu, S.W.; Yuan, X.-C. Sub-100nm resolution PSIM by utilizing modified optical vortices with fractional topological charges for precise phase shifting. *Optics Express* **2015**, 23, 30143-30148.

(10) Chen, L. X.; Lei, J.J.; Romero, J. Quantum digital spiral imaging. *Light: Science & Applications* **2014**, 3, e153.

(11) Wang, J.; Yang, J.-Y.; Fazal, I.M.; Ahmed, N.; Yan, Y.; Huang, H.; Ren, Y.; Yue, Y.; Dolinar, S.; Tur, M.; Willner, A.E. Terabit free-space data transmission employing orbital angular momentum multiplexing. *Nature Photonics* **2012**, 6, 488–496.

(12) Ruffato, G.; Massari, M.; Romanato, F. Diffractive optics for combined spatial-and mode-division demultiplexing of optical vortices: design, fabrication and optical characterization. *Scientific reports* **2016**, 6, 24760.

(13) Wang, X.; Nie, Z.; Liang, Y.; Wang, J.; Li, T.; Jia, B. Recent advances on optical vortex generation. *Nanophotonics* **2018**, 7, 1533-1556.

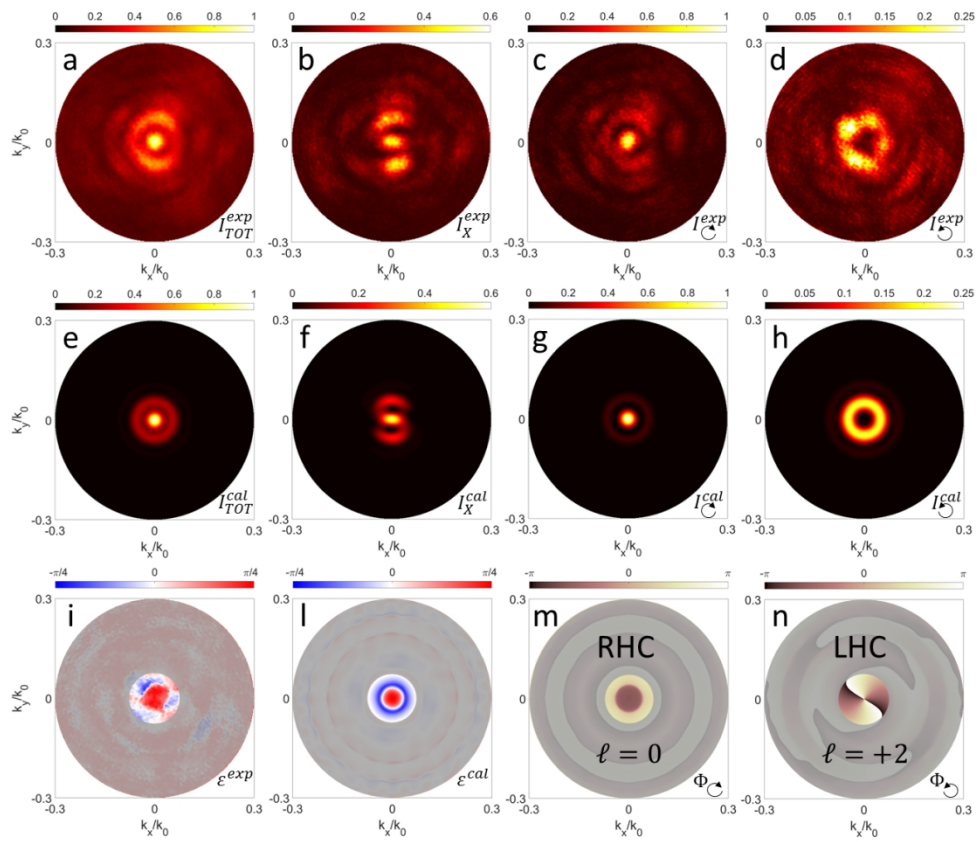16

(14) Marrucci, L.; Manzo, C.; Paparo, D. Optical Spin-to-Orbital Angular Momentum Conversion in Inhomogeneous Anisotropic Media. *Physical Review Letters* **2006**, 96, 163905.

(15) Moreno, I.; Davis, J.; Ruiz, I.; Cottrell, D. Decomposition of radially and azimuthally polarized beams using a circular-polarization and vortex-sensing diffraction grating. *Optics Express* **2010**, 18, 7173-7183.

(16) Cardano, F.; Karimi, E.; Slussarenko, S.; Marrucci, L.; de Lisio. C.; Santamato, E. Polarization pattern of vector vortex beams generated by q-plates with different topological charges. *Applied Optics* **2012**, 51, C1-C6.

(17) Genevet, P.; Lin, J.; Kats, M.A.; Capasso, F. Holographic detection of the orbital angular momentum of light with plasmonic photodiodes. *Nature Communications* **2012**, 3, 1278.

(18) Lin, J.; Genevet, P.; Kats, M.A.; Antoniou, N.; Capasso, F. Nanostructured holograms for broadband manipulation of vector beams. *Nano Letters* **2013**, 13, 4269-4274.

(19) Zhan, A.; Colburn, S.; Trivedi, R.; Fryett, T.K.; Dodson, C.M.; Majumdar, A. Low-Contrast Dielectric Metasurface Optics. *ACS Photonics* **2016**, 3, 209-214.

(20) Zhou, Y.; Gao, H.; Teng, J.; Luo, X.; Hong, M. Orbital angular momentum generation via a spiral phase microsphere. *Optics Letters* **2018**, 43, 34-37.

(21) Yue, F.; Wen, D.; Xin, J.; Gerardot, B.D.; Li, J.; Chen, X. Vector Vortex Beam Generation with a Single Plasmonic Metasurface. *ACS Photonics* **2016**, 3, 1558−1563.

(22) Huang, Y.-W.; Rubin, N.A.; Ambrosio, A.; Shi, Z.; Devlin, R.C.; Qiu, C.-W.; Capasso, F. Versatile total angular momentum generation using cascaded J-plates. *Optics Express* **2019**, 27, 7469-7484.

(23) Bliokh, K.Y.; Rodríguez-Fortuño, F.J.; Nori, F.; Zayats, A.V. Spin–orbit interactions of light. *Nature Photonics* **2015**, 9, 796–808.

(24) Bouchard, F.; De Leon, I.; Schulz, S.A.; Upham, J.; Karimi, E.; Boyd, R.W. Optical spin-to-orbital angular momentum conversion in ultra-thin metasurfaces with arbitrary topological charges. *Applied Physics Letters* **2014**, 105, 101905.

(25) Maguid, E.; Chriki, R.; Yannai, M.; Kleiner, V.; Hasman, E.; Friesem, A.A.; Davidson, N. Topologically Controlled Intracavity Laser Modes Based on Pancharatnam-Berry Phase. *ACS Photonics* **2018**, 551817-1821.

(26) Shalaev, M.I.; Sun, J.; Tsukernik, A.; Pandey, A.; Nikolskiy, K.; Litchinitser, N.M. High-Efficiency All-Dielectric Metasurfaces for Ultracompact Beam Manipulation in Transmission Mode. *Nano Letters* **2015**, 15, 6261-6266.
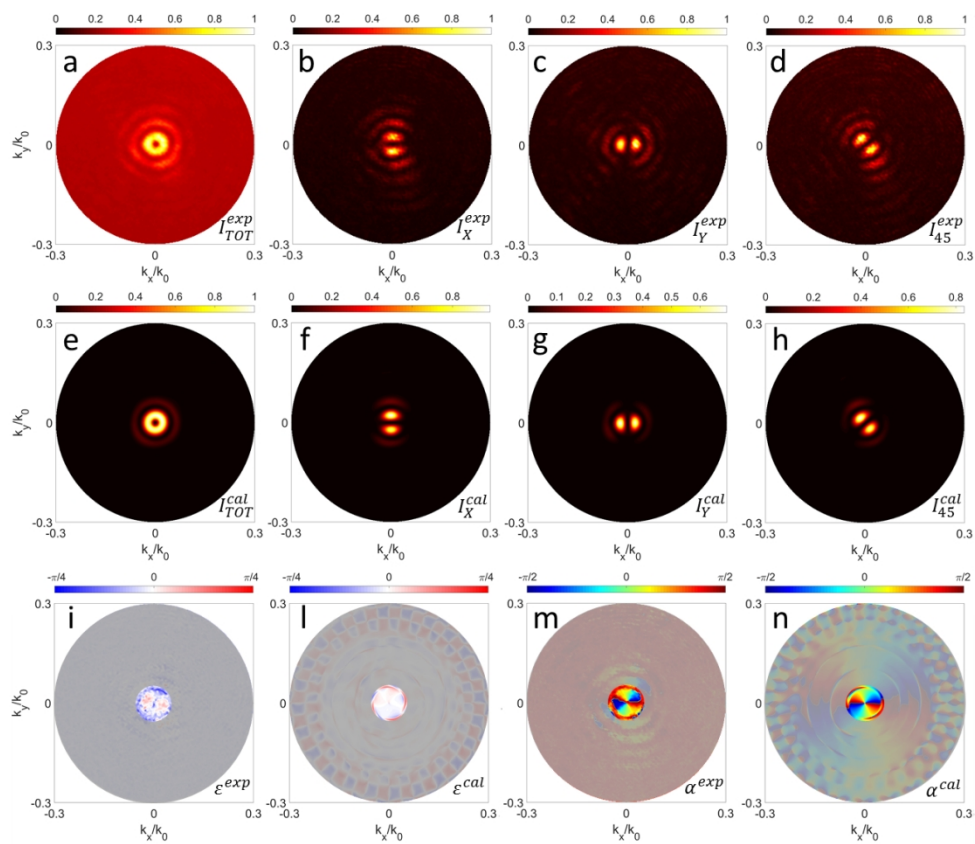
17

(27) Ou, K.; Li, G.; Li, T.; Yang, H.; Yu, F.; Chen, J.; Zhao, Z.; Cao, G.; Chen, X.; Lu, W. High efficiency focusing vortex generation and detection with polarization-insensitive dielectric metasurfaces. *Nanoscale* **2018**, 10, 19154-19161.

(28) Yang, Y.; Wang, W.; Moitra, P.; Kravchenko, I.I.; Briggs, D.P.; Valentine, J. Dielectric Meta-Reflectarray for Broadband Linear Polarization Conversion and Optical Vortex Generation. *Nano Letters* **2014** 14, 1394-1399.

(29) Wang, Z.; Wang, Y.; Adamo, G.; Teng, J.; Sun, H. Induced Optical Chirality and Circularly Polarized Emission from Achiral CdSe/ZnS Quantum Dots via Resonantly Coupling with Plasmonic Chiral Metasurfaces. *Laser & Photonics Reviews* **2019**, 13, 1800276.

(30) Rui, G.; Nelson, R.L.; Zhan, Q. Beaming photons with spin and orbital angular momentum via a dipole-coupled plasmonic spiral antenna," *Optics Express* **2012**, 18819-18826.

(31) Yu, H.; Zhang, H.; Wang, Y.; Han, S.; Yang, H.; Xu, X.; Wang, Z.; Petrov, V.; Wang, J. Optical orbital angular momentum conservation during the transfer process from plasmonic vortex lens to light. *Scientific Reports* **2013**, 3, 3191.

(32) Jiang, Q.; Pham, A.; Berthel, M; Huant, S.; Bellessa, J.; Genet, C.; Drezet, A. Directional and Singular Surface Plasmon Generation in Chiral and Achiral Nanostructures Demonstrated by Leakage Radiation Microscopy. *ACS Photonics* **2016**, 3, 1116-1124.

(33) Gorodetski, Y.; Shitrit, N.; Bretner, I.; Kleiner, V.; Hasman, E. Observation of Optical Spin Symmetry Breaking in Nanoapertures. *Nano Letters* **2009**, 9, 3016-3019.

(34) Zhang, B.; Hu, C.; Tang, B.; Hao, J.; Zhang, X.; Sun, M.; Ding, J. Chiral plasmonic lens with Archimedes-spiral distributed nanoslits. *Journal of Nanophotonics* **2019**, 13, 026008.

(35) Gorodetski, Y.; Drezet, A.; Genet, C.; Ebbesen, T.W. Generating Far-Field Orbital Angular Momenta from Near-Field Optical Chirality. *Physical Review Letters* **2013**, 110, 203906.

(36) Robertson, W.M.; May, M.S. Surface electromagnetic wave excitation on one-dimensional photonic band-gap arrays. *Applied Physics Letters* **1999**, 74, 1800.

(37) Liscidini, M.; Galli, M.; Patrini, M.; Loo, R.W.; Goh, M.C.; Ricciardi, C.; Giorgis, F.; Sipe, J. E. Demonstration of diffraction enhancement via Bloch surface waves in a-SiN:H multilayers. *Applied Physics Letters* **2009**, 94, 043117.

(38) Sinibaldi, A.; Fieramosca, A.; Rizzo, R.; Anopchenko, A.; Danz, N.; Munzert, P.; Magistris, C.; Barolo, C.; Michelotti, F. Combining label-free and fluorescence operation of Bloch surface wave optical sensors. *Optics Letters* **2014**, 39, 2947-2950.

(39) Wang, M.: Zhang, H.; Kovalevich, T.; Salut, R.; Kim, M.-S.; Suarez, M.A.; Bernal, M.-P.; Herzig, H.-P.; Lu, H.; Grosjean, T. Magnetic spin–orbit interaction of light. *Light Science and Applications* **2018**, 7, 24.
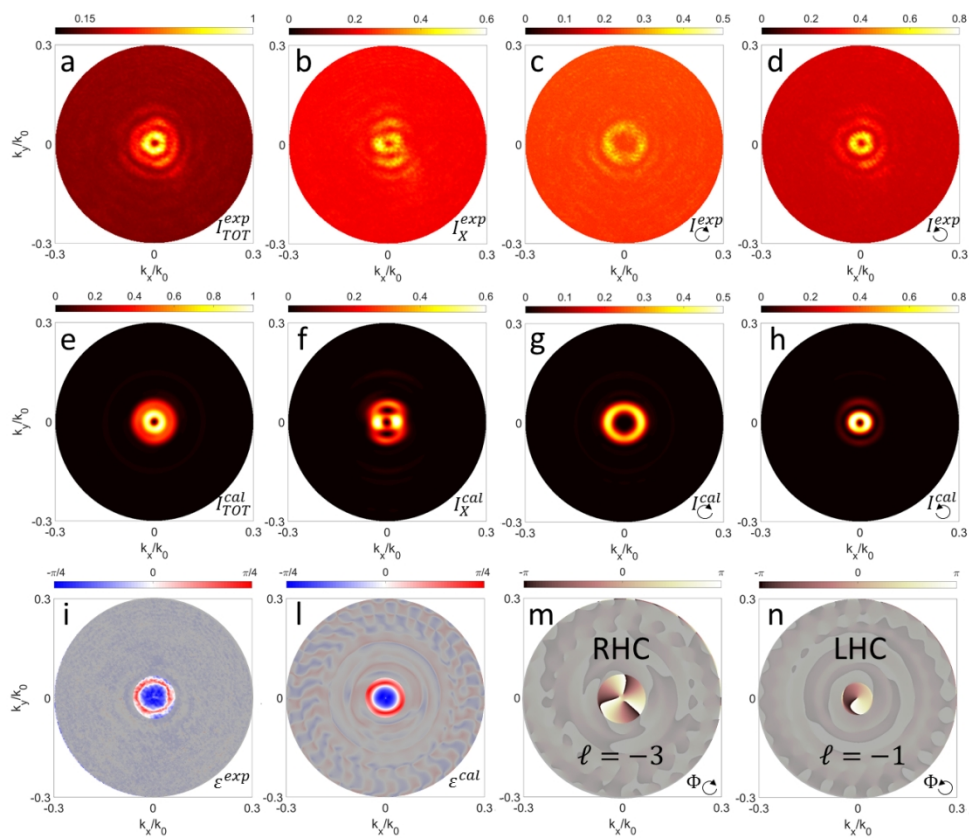
18

(40) Angelini, A.; Barakat, E.; Munzert, P.; Boarino, L.; De Leo, N.; Enrico, E.; Giorgis, F.; Herzig, H.P.; Pirri, C.F.; Descrovi, E. Focusing and extraction of light mediated by Bloch surface waves. *Scientific Reports* **2014**, 4, 5428.

(41) Kim, H.; Park, J.; Cho, S.-W.; Lee, S.-Y.; Kang, M.; Lee, B. Synthesis and Dynamic Switching of Surface Plasmon Vortices with Plasmonic Vortex Lens. *Nano Letters* **2010**, 10, 529-536.

(42) Angelini, A.; Enrico, E.; de Leo, N.; Munzert, P.; Boarino, L.; Michelotti, F.; Giorgis, F.; Descrovi, E. Fluorescence diffraction assisted by Bloch surface waves on a one-dimensional photonic crystal. *New Journal of Physics* **2013**, 15, 073002

(43) Rui, G.; Abeysinghe, D.C.; Nelson, R.L.; Zhan, Q. Demonstration of beam steering via dipole-coupled plasmonic spiral antenna. *Scientific Reports* **2013**, 3, 2237.

(44) Angelini, A.; Munzert, P.; Enrico, E.; De Leo, N.; Scaltrito, L.; Boarino, L.; Giorgis, F.; Descrovi, E. Surface-Wave-Assisted Beaming of Light Radiation from Localized Sources. *ACS Photonics* **2014**, 1, 612–617.

(45) Röhrich, R.; Hoekmeijer, C.; Osorio, C.I.; Koenderink, A.F. Quantifying single plasmonic nanostructure far-fields with interferometric and polarimetric k-space microscopy. *Light-Science & Applications* **2018**, 7, 65.

(46) Pellegrini, G.; Finazzi, M.; Celebrano, M.; Duò, L.; Biagioni, P. Chiral surface waves for enhanced circular dichroism. *Physical Review B* **2017**, 95, 241402.

(47) Angelini, A. Resonant evanescent complex fields on dielectric multilayers. *Optics Letters* **2015**, 40, 5746-5749.

(48) Liscidini, M.; Galli, M.; Shi, M.; Dacarro, G.; Patrini, M.; Bajoni, D.; Sipe, J.E. Strong modification of light emission from a dye monolayer via Bloch surface waves. *Optics Letters* **2009**, 34, 2318-2320.

(49) Badugu, R.; Mao, A.; Blair, S.; Zhang, D.; Descrovi, E.; Angelini, A.; Huo, Y.; Lakowicz, J.R. Bloch Surface Wave-Coupled Emission at Ultra-Violet Wavelengths. *Journal of Physical Chemistry C* **2016**, 120, 28727-28734.

(50) Stella, U.; Boarino, L.; de Leo, N.; Munzert, P.; Descrovi, E. Enhanced directional light emission assisted by resonant Bloch Surface Waves in circular cavities. *ACS Photonics* **2019**, 6, 2073-2082.

(51) Pham, A.; Berthel, M.; Jiang, Q.; Bellessa, J.; Huant, S.; Genet, C.; Drezet, A. Chiral optical local density of states in a spiral plasmonic cavity. *Physical Review A* **2016**, 94, 053850.

(52) Pachidis, P.; Cote, B.M.; Ferry, V.E. Tuning the polarization and directionality of photoluminescence of achiral quantum dot films with chiral nanorod dimer arrays: implications for luminescent applications. *ACS Applied Nano Materials* **2019**, 2, 5681-5687.

509 **GRAPHICAL TOC ENTRY**

510

a

b

Ta$_2$O$_5$ SiO$_2$ PMMA

Vortex Beam

$\vec{k}_{BSW}$ ϑ_c

$\vec{k}_{BSW}$

Vortex Beam

BSW

Glass   Air

Circular Polarization

BS Objective

NA=1.49

QW$_2$

LP$_2$

L4

BFP

CMOS camera

Mirror

L3

BB on XY stage

2f

L2

Circular Polarization

QW$_1$

LP$_1$

L1

Linear Polarization

TEM$_{00}$ Laser Source

Piezo stage

c

Λ=450 nm

PMMA 75 nm

6 μm

SiO$_2$ 127 nm

SiO$_2$ 137 nm

Glass

Ta$_2$O$_5$ 95 nm

81x44mm (300 x 300 DPI)